

Bulk Bi-Sb polycrystals underpinned by high electron/phonon mean free path ratio enabling thermoelectric cooling under 77 K

Received: 16 December 2024

Accepted: 21 March 2025

Published online: 14 April 2025

Check for updates

Xiaowei Wu^{1,2}, Zhen Fan¹, Hangtian Zhu¹, Tianyu Wang³, Meng Liu¹, Jun Li¹, Nan Chen^{1,2}, Qilun Liu^{1,2}, Zhen Lu¹, Guodong Li¹, Xin Qian³, Te-Huan Liu³✉, Ronggui Yang⁴, Xiaoyan Niu⁵, Qi Zhao⁵, Zhiliang Li⁵, Shufang Wang⁵ & Huaizhou Zhao¹✉

Bi-Sb alloy, as a promising thermoelectric material at cryogenic temperatures, has seen stagnant progress due to challenges in understanding the transport behaviors of energy carriers, and difficulties in synthesizing high-homogeneity, large-grain samples. In this study, an inherent electron-phonon decoupling in Bi-Sb is revealed using the first-principles calculations based on the virtual crystal approximation. The mean free path of the dominant electrons ($\lambda_{\text{ele}} \sim 10^3$ nm) is found of two orders of magnitude larger than that of phonons ($\lambda_{\text{ph}} \sim 10^1$ nm), suggesting that a grain size greater than 10 μm would be favorable for thermoelectric transport. Bulk Bi-Sb polycrystals with highly elemental homogeneity and large grain size (~ 80 μm) are successfully synthesized through an ultra-fast quenching method combined with annealing, delivering superior thermoelectric performance. A prototype module based on the $\text{Bi}_{0.88}\text{Sb}_{0.12}$ polycrystal, with a ZT_{max} of 0.48 at 150 K, is fabricated and demonstrates a ΔT_{max} of 4 K at a T_{h} of 75 K. This marks the first report of n-p paired thermoelectric cooling modules operating below liquid nitrogen temperature.

With increasing demands in space exploration, optoelectronics, and medical industry, solid-state cooling techniques have developed rapidly in recent years. Notable advancements have been made particularly in magnetocaloric^{1,2}, electrocaloric^{3,4}, elastocaloric^{5,6}, and laser cooling technologies^{7,8}. Among these, thermoelectric (TE) cooling based on the Peltier effect has seen significant progress since the 1960s owing to its unique advantages, including high power density, fast response, reliability, and precise temperature control over a wide range⁹. Thermoelectric cooling (TEC) modules are widely used in cryogenic applications such as cooling superconducting magnets in Magnetic Resonance Imaging systems and maintaining low temperatures for infrared sensors in space exploration¹⁰. The performance of

TEC modules is primarily determined by the figure of merit (ZT) of the TE material used, defined as $ZT = \sigma S^2 T / \kappa$, where σ is the electrical conductivity, S is the Seebeck coefficient, κ is the total thermal conductivity, and T is the absolute temperature¹¹. Bi_2Te_3 exhibits a high ZT of -1.0 for both n and p types at near-room temperatures, making it the dominant commercial TE material for decades¹²⁻¹⁴. However, its low TE performance at cryogenic temperatures below 200 K limits the cooling efficiency of Bi_2Te_3 -based TE coolers, as evidenced by a reduced ZT value, which highlights the urgent need for the development of high-performance TE materials for deep-temperature cooling applications.

Among the proposed cryogenic TE materials, such as FeSb_2 ¹⁵, CeCu_6 ¹⁶, $\text{Mg}_3(\text{Bi}, \text{Sb})_2$ ^{17,18}, CsBi_4Te_6 ¹⁹, Bi-Sb alloys have emerged as the

¹Beijing National Laboratory for Condensed Matter Physics, Institute of Physics, Chinese Academy of Sciences, Beijing, China. ²School of Physical Science, University of Chinese Academy of Sciences, Beijing, China. ³School of Energy and Power Engineering, Huazhong University of Science and Technology, Wuhan, China. ⁴College of Engineering, Peking University, Beijing, China. ⁵Hebei Key Lab of Optic-Electronic Information and Materials, Key Laboratory of High-Precision Computation and Application of Quantum Field Theory of Hebei Province, College of Physics Science and Technology, Hebei University, Baoding, China. ✉e-mail: thliu@hust.edu.cn; hzhao@iphy.ac.cn

best n-type TE materials at low temperatures, with single crystals exhibiting a maximum ZT value of -0.55 at 125 K ^{20,21}. Bi-Sb alloys crystallize in an $R\bar{3}m$ rhombohedral structure, with distinct carrier transport along the binary and trigonal directions. It has been reported that the electronic band structure of Bi-Sb alloys is highly sensitive to mass composition, where a narrow band gap forms only when the fraction of Sb (x) falls within the range from 7% to 22%^{22,23}, as shown in Supplementary Fig. 1. The band gap reaches 20 to 30 meV when x is between 12% and 15%, leading to a favorable Seebeck coefficient and optimal TE performance²⁴. However, due to the existence of a large solubility gap in the Bi-Sb binary phase diagram²⁵, phase segregation usually occurs during cooling and crystallization from the melt. As a result, synthesizing atomically uniform Bi-Sb alloys, whether as single crystals or polycrystals, is challenging²⁶, not to mention the poor mechanical strength of the single crystal due to the van der Waals binding in its layered structure. On the other hand, the challenges in modeling the TE properties of semimetal alloys make the coupling between electron and phonon transport in Bi-Sb alloys difficult to fully understand, hindering the development of effective strategies for enhancing thermoelectric performance. These limitations severely restrict the application of existing bulk Bi-Sb single and polycrystals, leading to inferior TE performance in cryogenic TEC.

Results

Thermoelectric figure of merit and cooling performance of bulk Bi-Sb polycrystals

In this study, an ultra-fast quenching technique, commonly used in the synthesis of metallic glass²⁷, combined with annealing, was adopted to prepare high-homogeneous, large-grain Bi-Sb polycrystals. These samples not only exhibited TE performance comparable to that of high-quality single crystals²⁸, but also demonstrated remarkable mechanical characteristics with compressive strengths exceeding 200 MPa (Supplementary Fig. 2). As shown in Fig. 1a, for a typical $\text{Bi}_{0.88}\text{Sb}_{0.12}$ polycrystal, the maximum figure of merit (Z) in the studied temperatures was measured at $4.0 \times 10^{-3}\text{ K}^{-1}$ at 100 K without a magnetic field, and $3.5 \times 10^{-3}\text{ K}^{-1}$ at 175 K under a 0.5 T magnetic field. The results indicate that at temperatures below 175 K, the Z value of the $\text{Bi}_{0.88}\text{Sb}_{0.12}$ polycrystal surpasses that of the n-type $\text{Bi}_2(\text{Te},\text{Se})_3$ and state-of-the-art $\text{Mg}_3(\text{Bi},\text{Sb})_2$, highlighting its unique potential for cryogenic TE cooling. This excellent TE performance can be attributed

to the improved quenching and crystallization during the synthesis process, which enabled the production of highly uniform elemental distribution and large grain sizes. These effects on TE transport properties will be further explained in the calculation section.

A uni-couple TEC module was fabricated using the as-annealed $\text{Bi}_{0.88}\text{Sb}_{0.12}$ polycrystal as the n-type leg and the commercial $\text{Bi}_{0.5}\text{Sb}_{1.5}\text{Te}_3$ as the p-type leg. The cooling temperature difference (ΔT) of the module was measured across a broad range of low temperatures. As shown in Fig. 1b, at a hot-end temperature (T_h) of 200 K, the ΔT of the TE module reached 30 K, which approaches the theoretical value. As T_h decreased, a ΔT of 4 K was achieved at $T_h = 75\text{ K}$. These experimental results validate the excellent TE performance of the $\text{Bi}_{0.88}\text{Sb}_{0.12}$ -based module at very low temperatures. Compared to the results of a fully Bi_2Te_3 -based TEC module reported by Yim²⁹, our $\text{Bi}_{0.88}\text{Sb}_{0.12}$ -based module exhibited significantly larger ΔT particularly when T_h is below 175 K, which aligns with the curves of Z value presented in Fig. 1a. Since 1968, the best cooling performance in the deep-temperature regime has been $\Delta T = 2.5\text{ K}$ at $T_h = 79\text{ K}$ ²⁹. Our $\text{Bi}_{0.88}\text{Sb}_{0.12}$ -based module has rewritten this record, and for the first time, it demonstrates the capability for deep-temperature cooling below liquid nitrogen temperature using an n-p paired configuration. While single-leg TEC modules incorporating high-temperature superconductors as passive legs have demonstrated better low-temperature cooling performance^{30,31}, n-p paired TE modules made from polycrystalline materials provide greater value in practical applications.

First-principles calculations based on the VCA for Bi-Sb alloys

To elucidate the outstanding TE performance of the $\text{Bi}_{0.88}\text{Sb}_{0.12}$ polycrystal, first-principles calculations based on the virtual crystal approximation (VCA) were employed to investigate electron and phonon transport in the alloy system. As an example, the phonon spectrum of $\text{Bi}_{0.88}\text{Sb}_{0.12}$ obtained using the VCA is shown in Supplementary Fig. 3. The phonon frequencies lie between those of pure Bi and Sb crystals, being closer to Bi, which demonstrates the validity of the VCA. For electron transport, the scatterings due to phonons and alloy disorders were considered. The localized disturbances in crystal potential caused by Bi and Sb alloy atoms (Supplementary Fig. 4) were factored in constructing the electron- and hole-alloy coupling matrices. For phonon transport, three-phonon, four-phonon, and phonon-alloy scatterings were included. Phonon scattering by alloy disorder

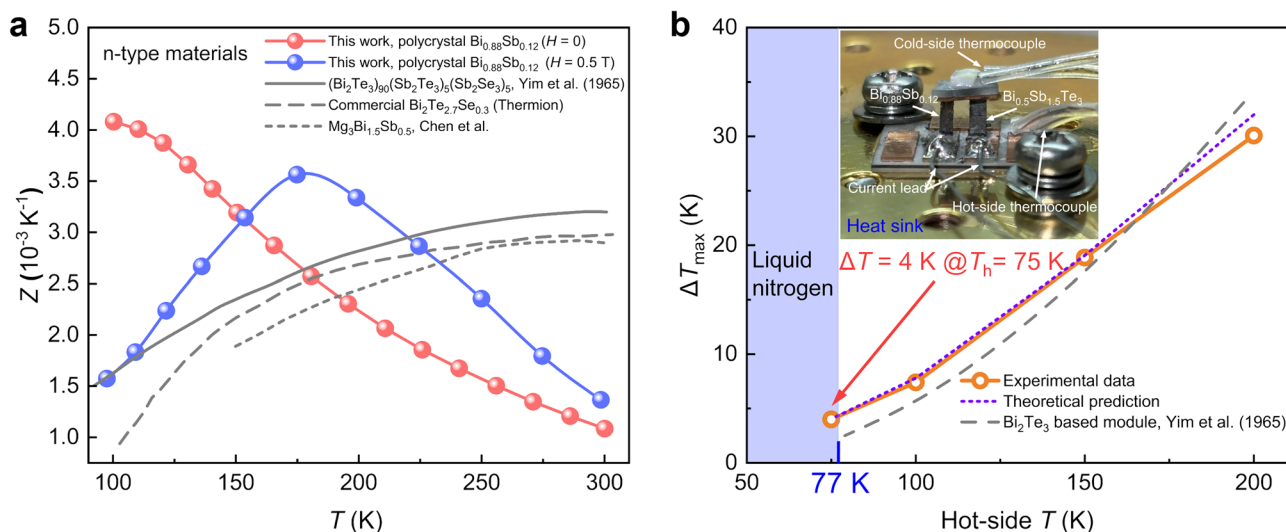


Fig. 1 | Thermoelectric performance of bulk $\text{Bi}_{0.88}\text{Sb}_{0.12}$ polycrystals and cooling performance of the prototype TEC module. **a The measured temperature-dependent figure of merit, Z , for $\text{Bi}_{0.88}\text{Sb}_{0.12}$ polycrystals with 0.5 T and without a magnetic field. The measured Z is compared to that of other**

prevailing TE materials^{18,29}. **b** The maximum cooling temperature differences between the hot and cold sides of the module as a function of T_h . The inset shows the experimental setup for the thermoelectric cooling measurement with a uni-couple module consisting of n-type $\text{Bi}_{0.88}\text{Sb}_{0.12}$ and p-type $\text{Bi}_{0.5}\text{Sb}_{1.5}\text{Te}_3$ legs.

was modeled using a mass disorder approach, with coupling matrices computed via the Pearson deviation coefficient³². Figure 2a shows the normalized accumulation of electrical and thermal conductivity as a function of the maximum mean free paths (MFPs) of the corresponding carriers. The lower and upper characteristic MFPs for electrons are 55 and 1700 nm, respectively, while for phonons, they are 2 and 20 nm. Electrons and phonons with MFPs within these characteristic ranges contribute approximately 80% of the total electrical and thermal conductivity. This reveals an interesting feature that the MFP of the predominant electrons in the Bi_{0.88}Sb_{0.12} alloy is approximately two orders of magnitude greater than that of the phonons, which is distinct from other typical TE materials such as PbTe³³, SnSe³⁴, SnTe³⁵, and Si³⁶, where the phonon MFPs are comparable to or larger than the electron MFPs. This inherent electron-phonon decoupling can be observed from room to cryogenic temperatures (Fig. 2b), where the spectral electrical and lattice thermal conductivities exhibit a redshift as the temperature decreases, caused by the fewer phonon occupations that reduce the electron and phonon scatterings.

This unique high $\lambda_{\text{ele}}/\lambda_{\text{ph}}$ ratio reveals an inherent decoupling of electron and phonon transport in Bi-Sb alloys, which can be attributed to two main factors. First, for a “perfect Bi_{0.88}Sb_{0.12} crystal” (considering only the electron-phonon and phonon-phonon scattering), our first-principles calculations show good electrical conductivity ($1.25 \times 10^6 \text{ S}\cdot\text{m}^{-1}$) and low lattice thermal conductivity ($6.74 \text{ W}\cdot\text{m}^{-1}\cdot\text{K}^{-1}$) at 100 K. Although the alloy scattering was artificially excluded, the lattice thermal conductivity is still comparable to the values of real Bi₂Te₃ crystals, which range from 4 to $6 \text{ W}\cdot\text{m}^{-1}\cdot\text{K}^{-1}$ at 100 K³⁷. A comparison of the room-temperature thermal conductivity with other commonly used thermoelectric materials is provided in Supplementary Table 1. This arises from a narrow band gap that facilitates the probability of electrons occupying conduction states, as well as from the intrinsically high lattice anharmonicity and low phonon group velocity (Supplementary Fig. 3 and Supplementary Table 2). The high lattice anharmonicity in Bi-Sb solids arises from the existence of resonant bonds³⁸, which form because the chemical bonds are primarily composed of *p*-electrons to satisfy the sixfold coordination required by the cubic crystal structure³⁹. Its relatively low intrinsic thermal conductivity, along with the significant thermal resistance contributed by four-phonon scattering, further supports the high anharmonicity in the BiSb system. The calculated phonon group velocity along the high-symmetry directions is provided in Supplementary Table 2. These predictions are in good agreement with the experimental measurements ($\sim 1200 \text{ m}\cdot\text{s}^{-1}$ for TA phonon and $\sim 2500 \text{ m}\cdot\text{s}^{-1}$ for LA phonon, shown in Supplementary Fig. 5), and comparable to those of Bi₂Te₃ (ranging from 1 to 3 THz⁴⁰). Additionally, the alloy scattering has a much greater effect on reducing lattice thermal conductivity than on electrical conductivity. At 100 K, over 80% of the lattice thermal conductivity in Bi_{0.88}Sb_{0.12} is contributed by phonons with frequencies greater than 0.8 THz when only the phonon-phonon scattering is considered. In this frequency range, the phonon-alloy scattering rate is significantly higher than the three- and four-phonon scattering rates (Fig. 2c and Supplementary Fig. 6). Accounting for alloy disorder in heat conduction, the calculations show a 69% reduction in lattice thermal conductivity at 100 K (from 6.74 to $2.10 \text{ W}\cdot\text{m}^{-1}\cdot\text{K}^{-1}$, Supplementary Fig. 7). In contrast, it has a weaker effect on electron transport compared to phonons (Fig. 2d and Supplementary Fig. 8). The experimentally measured carrier concentration is $3.2 \times 10^{17} \text{ cm}^{-3}$ at 100 K, corresponding to a Fermi level of 7.1 meV above the conduction band minimum (CBM). Given that the average thermal excitation energy ($k_B T$) at this temperature is about 8.6 meV, electron transport is primarily dominated by electrons within a narrow energy window near the CBM. It can be seen that the electron-alloy scattering rates are comparable to or even lower than the charge-phonon scattering rates near the CBM. The charge-alloy interaction becomes significant only at higher energies, where electron occupancy

is very low. Our calculations show that alloy scattering reduces electrical conductivity by 33% (from 1.25×10^6 to $8.39 \times 10^5 \text{ S}\cdot\text{m}^{-1}$). These transport characteristics further increase the $\lambda_{\text{ele}}/\lambda_{\text{ph}}$ ratio in the Bi-Sb alloy.

Grain boundary scattering plays another important role in affecting the TE transport properties, as previously mentioned. It is worth noting that the calculated transport properties presented here represent an average value across all crystallographic axes, specifically $(2 \times \text{binary} + \text{trigonal})/3$, because the prepared Bi_{0.88}Sb_{0.12} crystals are polycrystalline, with the orientations of individual grains being randomly distributed. Our calculations show that the effect of grain size on thermal conductivity becomes minimal once the characteristic length reaches the micrometer scale (Fig. 2e for average values and Supplementary Fig. 9 for binary and trigonal directions). This is attributed to the strong lattice anharmonicity and phonon-alloy scattering inherent in the Bi-Sb alloy, which restricts the MFPs of the dominant phonons to several tens of nanometers, preventing significant boundary scattering. As expected, a larger grain size improves electrical conductivity due to reduced boundary scattering. However, the Seebeck coefficient decreases slightly with increasing grain size (Supplementary Fig. 10). This decrease is attributed to the “electron MFP filtering effect” in semiconductors with non-parabolic bands³⁵. This mechanism, which was proposed to explain the Seebeck coefficient exceeding its bulk limit in small grain sizes, also applies here. As the grain size increases, the Seebeck coefficient decreases and eventually recovers the bulk limit. The explanation is as follows: in n-type semiconductors, when the Fermi level lies within the conduction band, electrons with energies below the Fermi level typically have longer MFPs and contribute a positive Seebeck coefficient, which is undesirable in n-type materials. In contrast, electrons with energies above the Fermi level generally have shorter MFPs and contribute a negative Seebeck coefficient. As the grain size increases, the long-MFP electrons experience less boundary scattering, allowing them to contribute more to the Seebeck coefficient, resulting in a lower Seebeck coefficient compared to those in smaller grains. Nevertheless, due to the much larger increase in electrical conductivity compared to the decrease in Seebeck coefficient, a larger power factor can still be found in a sample with larger grain size. The calculations suggest that a grain size greater than 10 μm is required to achieve satisfactory low-temperature electrical conductivity, while a grain size over 80 μm can yield electrical conductivity comparable to that of single-crystal Bi_{0.88}Sb_{0.12}. Elemental homogeneity in Bi-Sb polycrystals is also important in the electron transport properties, as studied in previous studies^{28,39}. Conversely, phase segregation may increase lattice thermal conductivity due to reduced mass-field fluctuations, which is detrimental to TE conversion.

Growth of Bi-Sb alloy polycrystals and microstructure characterizations

The analysis above highlights that optimizing grain size and improving elemental homogeneity are critical for enhancing the TE performance of Bi-Sb alloys. Regarding alloy synthesis, rapid quenching is commonly used to preserve the thermodynamic characteristics of materials from the preceding liquid phase⁴¹. Among the reported quenching techniques, melt spinning is widely employed to produce uniform metal alloy ribbons with a thickness of less than a few microns⁴², followed by hot pressing to solidify the melt-spun ribbons into bulk polycrystalline samples. However, this crystal growth method cannot produce sufficiently large grains and inevitably introduces oxidation at the grain boundaries, leading to a degradation of the electrical properties of Bi-Sb alloys. To overcome the limitations of melt spinning, in this study, a spray casting technique with an ultra-fast quenching rate ($\sim 10^3 \text{ K}\cdot\text{s}^{-1}$) was used to prepare Bi_{1-x}Sb_x polycrystals. This method allows the direct fabrication of bulk polycrystals with the desired size and dimensions, and is no need for additional grinding and

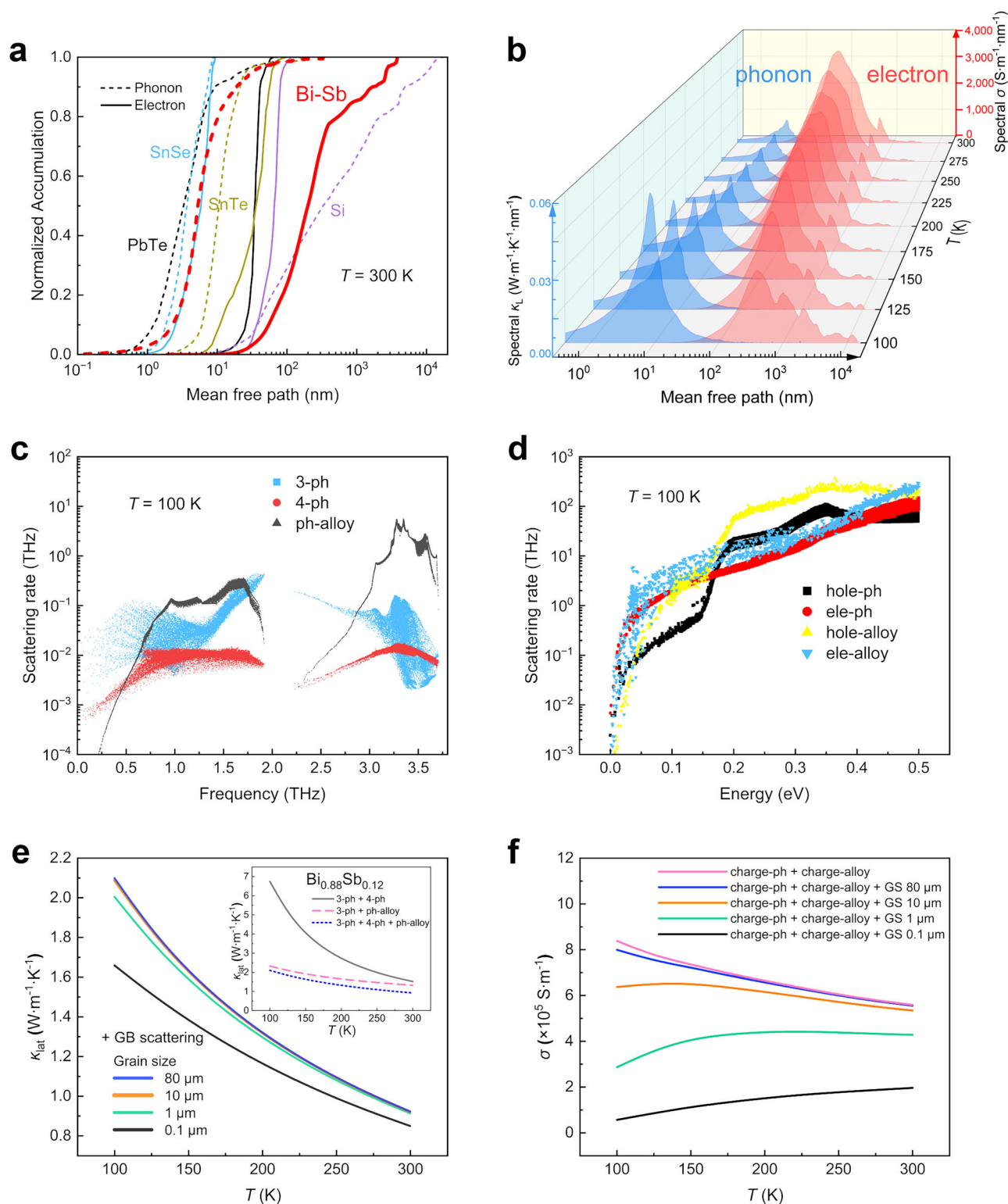


Fig. 2 | TE transport properties of the $\text{Bi}_{0.88}\text{Sb}_{0.12}$ alloy calculated by first-principles calculations based on the VCA. **a Normalized accumulation of lattice thermal conductivity (dashed) and electrical conductivity (solid lines) as a function of MFP at 300 K for $\text{Bi}_{0.88}\text{Sb}_{0.12}$ and four representative materials for comparison. The gray, blue, yellow, purple, and red lines, respectively, represent PbTe^{33} , SnSe^{34} , SnTe^{35} , Si^{36} , and $\text{Bi}_{0.88}\text{Sb}_{0.12}$ alloy (this work). **b** MFP-dependent spectral lattice thermal conductivity and electrical conductivity of $\text{Bi}_{0.88}\text{Sb}_{0.12}$ at different temperatures. **c** Phonon scattering rates due to the three-phonon (blue squares), four-phonon (red circles), and phonon-alloy (black triangles) interactions at $T = 100$ K.**

d Electron scattering rates due to the electron-phonon (red circles), hole-phonon (black squares), electron-alloy (blue inverted triangles) and hole-alloy (yellow triangles). The electrical properties are calculated at an n-type carrier concentration of $3.2 \times 10^{17} \text{ cm}^{-3}$, corresponding to the experimental result. Hole transport is considered due to the presence of bipolar effects. **e** Temperature-dependent lattice thermal conductivity of $\text{Bi}_{0.88}\text{Sb}_{0.12}$ polycrystals with varying grain sizes. The inset shows the change of the thermal conductivity as different levels of scattering mechanism were considered. **f** Temperature-dependent electrical conductivity of $\text{Bi}_{0.88}\text{Sb}_{0.12}$ polycrystals with varying grain sizes.

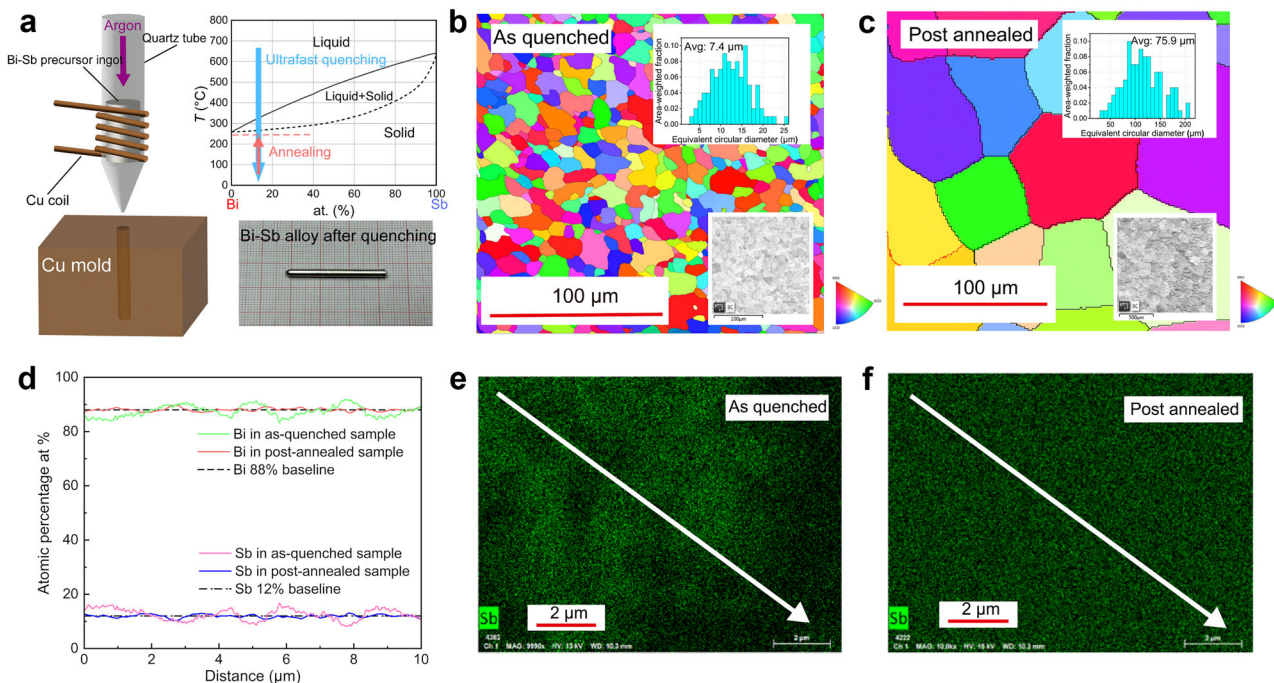


Fig. 3 | Synthesis and microstructural characterization of $\text{Bi}_{0.88}\text{Sb}_{0.12}$ polycrystals. **a** Schematic diagram illustrating the ultra-fast quenching process, the corresponding Bi-Sb binary phase diagram, and a photo image of the quenched sample. **b** EBSD image of the as-quenched sample. **c** EBSD image of the sample after

annealing at 530 K for 7 days. **d** Elemental concentration profiles of Bi and Sb from EDS analysis along the white lines in **(e)** the as-quenched sample and **(f)** the annealed sample, respectively.

solidification steps. As illustrated in Fig. 3a, the pre-synthesized Bi-Sb was mounted into a quartz tube with a 0.5 mm diameter nozzle at the bottom, and then heated by induction to a temperature of approximately 200–300 K above the upper solid-liquid line in the Bi-Sb binary phase diagram. After heating for 30 s, the molten Bi-Sb was quenched inside a copper mold to room temperature within 200 ms. The resulting cylindrical Bi-Sb bar, with a diameter of 3 mm and a length of 30 mm, is shown in the bottom right of Fig. 3a. The morphology and grain size of the as-quenched Bi-Sb were characterized using electron back-scattering diffraction (Fig. 3b), showing an average grain size of approximately 7.4 μm , with irregular grain boundaries, and no discernible texture was observed based on the grain misorientation angle distribution (Supplementary Fig. 11). Subsequently, the as-quenched $\text{Bi}_{0.88}\text{Sb}_{0.12}$ sample was annealed at 530 K—20 K below the solid-liquid line in the phase diagram—for 7 days. As shown in Fig. 3c, the sample recrystallized and the average grain size increased to approximately 80 μm , more than 10 times the size of the as-quenched sample. This significant grain growth was also observed by SEM (Supplementary Fig. 12). In comparison, Bi-Sb polycrystals synthesized by conventional ball-milling and melt-spinning techniques typically yield much smaller grain sizes of only a few microns. These samples exhibit relatively low ZT values as a result of the low carrier mobility, which is caused by significant grain boundary scattering⁴³.

The annealing process can also improve the elemental homogeneity of the sample, which is critical for maintaining the desired band gap and maximizing phonon scattering in Bi-Sb alloys. As shown in Fig. 3d, e, the as-quenched sample exhibited rough compositional distribution, characterized by significant Bi (green) and Sb (pink line) fluctuations at the microscale. After annealing, the enhanced elemental homogeneity in $\text{Bi}_{0.88}\text{Sb}_{0.12}$ is observed, driven by thermal diffusion and grain growth, as demonstrated by the Bi (red) and Sb (blue line) distributions and the energy dispersive spectroscopy images in Fig. 3f. Supplementary Fig. 13a shows the X-ray diffraction patterns for various annealed $\text{Bi}_{1-x}\text{Sb}_x$ samples, where the sharp diffraction

peaks indicate large crystal sizes and high-quality crystallization across all samples, which is further supported by the transmission electron diffraction results shown in Supplementary Fig. 14. Notably, as Sb content increases, the peaks of XRD shift to higher angles, reflecting a decreased lattice constant, as shown in Supplementary Fig. 13b. This also demonstrates the compositional precision and uniformity of the $\text{Bi}_{1-x}\text{Sb}_x$ alloys prepared in this study.

Thermoelectric performance of $\text{Bi}_{1-x}\text{Sb}_x$ bulk polycrystals

A series of $\text{Bi}_{1-x}\text{Sb}_x$ compositions centered around $x = 0.12$ (0.06, 0.09, 0.12, 0.15, and 0.18) were prepared using the synthesis method we developed, optimal performance can be achieved after 7 days of annealing (Supplementary Fig. 15), during which homogeneity improves and grain size increases concurrently. These compositions were selected since $\text{Bi}_{0.88}\text{Sb}_{0.12}$ exhibits favorable TE transport properties⁴⁴. As shown in Fig. 4a, the electrical conductivity for $x = 0.09$ to 0.18 exhibits semiconductor properties, with conductivity initially increasing as the temperature rises and then decreasing as further temperature increases. The conductivity for $x = 0.06$ shows a monotonic decline across the measured range, which is linked to its low carrier excitation temperature due to its semi-metallic nature. In the low-temperature regime ($T < 200$ K), electrical conductivity initially decreases and then increases with increasing x . This behavior is primarily caused by the varying carrier concentrations and bipolar effects (Supplementary Figs. 16 and 17), both of which arise from the different band gaps of these compositions. A crossover occurs at $x = 0.12$ with the highest isotropic electrical conductivity of $6.8 \times 10^5 \text{ S}\cdot\text{m}^{-1}$ is observed at 175 K for this composition, as shown in Fig. 4a and Supplementary Fig. 18. Based on the temperature-dependent electrical conductivity, the band gap for each composition was calculated using the Arrhenius law, as presented in the inset of Fig. 4a. Notably, the band gap value of the $\text{Bi}_{1-x}\text{Sb}_x$ samples aligns well with results of single crystals obtained through angle-resolved photoemission spectroscopy⁴⁵, where a band gap of 15 meV was identified for

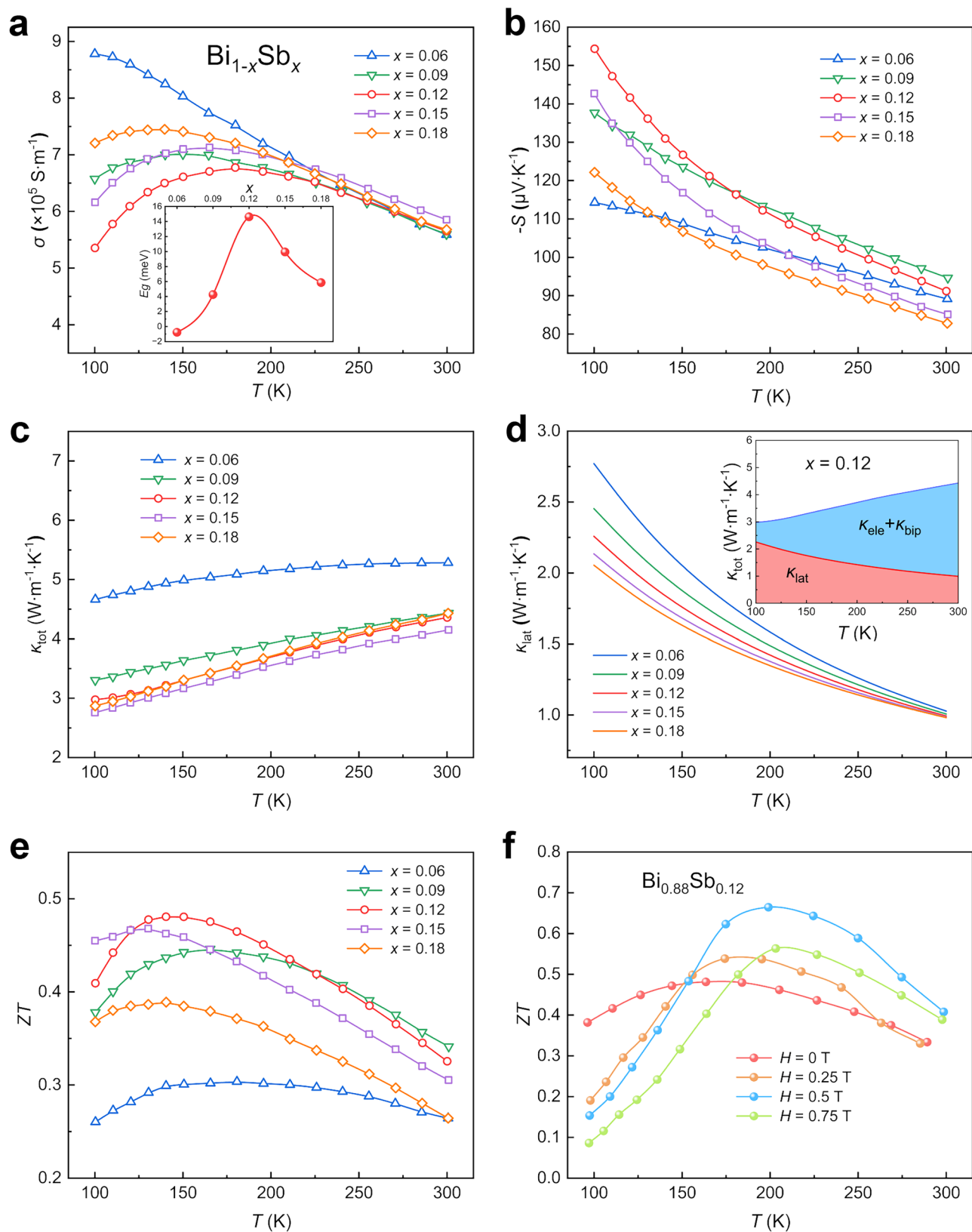


Fig. 4 | Temperature-dependent TE properties of the $\text{Bi}_{1-x}\text{Sb}_x$ polycrystals ($x = 0.06, 0.09, 0.12, 0.15$, and 0.18) prepared using the synthesis methods developed in this study. **a Electrical conductivity. The inset shows the band gap of the five samples, derived from the Arrhenius law and the measured electrical conductivity. **b** Seebeck coefficient. **c** Total thermal conductivity. **d** Lattice thermal**

conductivity obtained by the first-principles calculations. The inset shows the respective contributions of lattice and charge carriers, including electronic and bipolar transport, of the $\text{Bi}_{0.88}\text{Sb}_{0.12}$ polycrystal. **e** ZT . **f** ZT of the $\text{Bi}_{0.88}\text{Sb}_{0.12}$ polycrystal under different magnetic field intensities.

$\text{Bi}_{0.88}\text{Sb}_{0.12}$. Hall measurements were conducted to determine the carrier densities and mobilities. As shown in Supplementary Fig. 19, the Hall carrier densities of the $\text{Bi}_{1-x}\text{Sb}_x$ polycrystal initially decrease and then increase, with the lowest value occurring at $x=0.12$, corresponding to the largest band gap among the compositions. The carrier mobility follows a $T^{-1.5}$ trend across the studied temperature range, indicating that electron transport is primarily limited by acoustic-deformation-potential interactions rather than lattice defects or phase segregation, which typically cause deviations from the $T^{-1.5}$ relation, as reported in previous studies^{43,46}. This suggests that the samples synthesized by conventional methods contain significant crystal imperfections, and demonstrates the quality of our polycrystalline samples.

The Seebeck coefficient exhibits an opposite trend to electrical conductivity with varying x , consistent with previous reports⁴⁴ and our first-principles calculations (Supplementary Fig. 10). The maximum Seebeck coefficient of $-155 \mu\text{V}\cdot\text{K}^{-1}$ is observed in $\text{Bi}_{0.88}\text{Sb}_{0.12}$ at 100 K. Other compositions show lower Seebeck coefficients due to the reduced band gap, where bipolar transport becomes more significant as a result of the semi-metallic nature. The absolute value of the Seebeck coefficient decreases with increasing temperature due to thermal excitation resulting from the small bandgap in the Bi-Sb alloys. As shown in Supplementary Fig. 17a–c, the temperature dependence of carrier concentration and mobility indicates that the bipolar effect becomes more pronounced with increasing temperature across all three samples. Additionally, the ratio of hole conductivity to total conductivity (Supplementary Fig. 17d) shows that the bipolar transport effect is more significant in $\text{Bi}_{0.94}\text{Sb}_{0.06}$ and $\text{Bi}_{0.82}\text{Sb}_{0.18}$ compared to $\text{Bi}_{0.88}\text{Sb}_{0.12}$. These findings are consistent with the observed band gap and electrical transport properties: $\text{Bi}_{0.88}\text{Sb}_{0.12}$ exhibits a broader band gap than the other compositions, resulting in a weaker bipolar transport effect and a superior Seebeck coefficient among the materials studied.

The total thermal conductivity increases with increasing temperature, as shown in Fig. 4c. In contrast, the phonon component of total thermal conductivity decreases with rising temperature due to the enhanced lattice anharmonicity, as demonstrated by the first-principles results in Fig. 4d. Furthermore, the differences in lattice thermal conductivity for various x become very small at 300 K because alloy scattering is weakly dependent on temperature. As a result, the lattice heat conduction is primarily dominated by phonon-phonon interactions at elevated temperatures. The difference between the total and lattice thermal conductivity indicates a significant contribution of charge carriers to heat conduction in Bi-Sb alloys. The electron and bipolar thermal conductivities can be obtained by subtracting the first-principles lattice thermal conductivity from the total. As shown in the inset of Fig. 4d, charge carriers contribute approximately 30% to the total thermal conductivity in $\text{Bi}_{0.88}\text{Sb}_{0.12}$ polycrystals even at 100 K. The presented lattice thermal conductivity represents an average value from two binary and one trigonal direction, with detailed results for additional compositions provided in Supplementary Fig. 20. The averaged lattice thermal conductivity shows small variation within the range of $0.08 < x < 0.60$, with the lowest value at $1.98 \text{ W}\cdot\text{m}^{-1}\cdot\text{K}^{-1}$ ($x=0.3$) and the highest at $2.71 \text{ W}\cdot\text{m}^{-1}\cdot\text{K}^{-1}$ ($x=0.6$). For $\text{Bi}_{0.88}\text{Sb}_{0.12}$, the averaged lattice thermal conductivity is $2.26 \text{ W}\cdot\text{m}^{-1}\cdot\text{K}^{-1}$ at 100 K.

The temperature-dependent ZT values were obtained from the measured electrical conductivity, Seebeck coefficient, and total thermal conductivity, as shown in Fig. 4e. For all samples, the ZT values generally increase and then decrease as the temperature rises. Our experiments revealed that $\text{Bi}_{1-x}\text{Sb}_x$ with $x=0.09, 0.12$, and 0.15 possess better TE performance over the studied temperature range. Among these, $\text{Bi}_{0.88}\text{Sb}_{0.12}$ polycrystals displayed the highest ZT values from 125 K to 200 K, with a peak ZT of 0.48 at 150 K, which is comparable to the best-reported value for single-crystal Bi-Sb alloys^{20,21} ($ZT=0.55$ at 125 K). A strong interaction between TE transport properties and the Lorentz force has been demonstrated in Bi-Sb systems⁴⁷. Our results

show that introducing a magnetic field with $H < 0.75$ T can enhance the ZT values when the temperature exceeds 175 K, as shown in Supplementary Fig. 21. The peak ZT shifts to higher temperatures as the magnetic field intensity increases, with the largest enhancement observed at 200 K under 0.50 T, achieving a ZT of 0.68. The prepared $\text{Bi}_{0.88}\text{Sb}_{0.12}$ sample, used as the n-type leg, was integrated into a prototype TEC module, exhibiting the low interfacial electrical resistivity ($3.7 \mu\Omega\cdot\text{cm}^2$) and interfacial thermal resistivity ($0.14 \text{ mm}^2\cdot\text{K}\cdot\text{W}^{-1}$, Supplementary Fig. 22). This module demonstrated not only an excellent TE performance but also the capability for TE cooling below liquid nitrogen temperatures, as introduced earlier in this work.

Discussion

In summary, the excellent TE performance of Bi-Sb bulk polycrystals is attributed to the inherent decoupling of electron and phonon transport which enables a uniquely high $\lambda_{\text{ele}}/\lambda_{\text{ph}}$ ratio compared to the other commonly seen TE materials. A novel ultra-fast quenching method, combined with an annealing process, was developed to synthesize high-homogeneity $\text{Bi}_{1-x}\text{Sb}_x$ polycrystals with enlarged grain sizes of approximately 80 μm . The $\text{Bi}_{0.88}\text{Sb}_{0.12}$ polycrystal achieved a competitive ZT value of 0.48 at 150 K, comparable to the best-reported results for single crystals Bi-Sb alloys. As a proof of concept, a uni-couple TEC module based on the $\text{Bi}_{0.88}\text{Sb}_{0.12}$ polycrystal was fabricated, demonstrating superior TE performance compared to existing Bi_2Te_3 -based commercial TECs, and, for the first time, achieving solid-state cooling below liquid nitrogen temperatures in a TEC device with an n-p paired configuration. The developed experimental technique, along with the revealed physical characteristic of a high $\lambda_{\text{ele}}/\lambda_{\text{ph}}$ ratio, provides a new pathway for designing high-performance thermoelectrics.

Methods

Materials synthesis

Bi (pieces, 99.99%, Alfa Aesar) and Sb (pieces, 99.99%, Alfa Aesar) were weighed according to the nominal stoichiometry $\text{Bi}_{1-x}\text{Sb}_x$ where $x=0.06, 0.09, 0.12, 0.15$, and 0.18 . The raw elements with a total mass of 10 g were sealed in quartz tubes under a high vacuum of 10^{-4} Pa. The quartz tubes were heated to 973 K for 4 h, held at this temperature for another 2 h, and then cooled in iced water to obtain the precursor ingots for ultrafast quenching. The obtained ingot was placed into a quartz tube with a 0.5 mm diameter nozzle, melted by an induction coil under a 0.01 MPa argon atmosphere, and then sprayed into a copper mold under 0.04 MPa of argon pressure. For the annealing process, the Bi-Sb alloy rods obtained by ultrafast quenching were sealed in a quartz tube under a vacuum of 10^{-1} Pa and annealed at 533 K for 7 days.

Phase and microstructure characterization

Powder X-ray diffraction (Bruker D2 Phaser diffractometer) with Cu K α radiation ($\lambda=1.5418 \text{ \AA}$) was performed to analyze the phase composition at room temperature. Element distribution on the polished surface and the microstructure of the fracture surface were examined by a scanning electron microscope (SEM, S8100, Hitachi) equipped with Oxford energy-dispersive spectroscopy. To estimate the grain size and orientation, electron back-scattering diffraction was conducted using an Oxford Nordlys Max3 EBSD detector. Cryogenic Transmission Electron Microscopy (JEOL JEM-ARM200F NEOARM) at liquid nitrogen temperature was employed to obtain electron diffraction pattern images.

All transport properties of the samples were measured along the axial direction of the quenched sample rods. The total thermal conductivity and Seebeck coefficient were measured using a Thermal Transport Measurement System (TTMS, Multifields Tech.), and the electrical resistivity was measured using a Physical Properties Measurement System (PPMS, Quantum Design). The steady-state method was employed for measuring the total thermal conductivity and Seebeck coefficient. The thermoelectric transport properties under

magnetic fields and Hall coefficients, R_H , were also measured using the PPMS. The Hall carrier concentration, n_H , and the Hall carrier mobility, μ_H , were calculated by:

$$n_H = \frac{1}{eR_H}, \tag{1}$$

$$\mu_H = \sigma R_H, \tag{2}$$

where e is the electronic charge, σ is the electrical conductivity and R_H is the Hall coefficient.

Two-band transport model

The isotropic conductivity σ of m parallel-conducting carrier populations subject to a perpendicular magnetic field B_z is given by⁴⁸

$$\sigma_{xx}(B_z) = \sum_{i=1}^m \frac{\sigma_i}{1 + (\mu_i B_z)^2} = \sum_{i=1}^m \frac{q_i n_i \mu_i}{1 + (\mu_i B_z)^2}, \tag{3}$$

$$\sigma_{xy}(B_z) = \sum_{i=1}^m \frac{\sigma_i(\mu_i B_z)}{1 + (\mu_i B_z)^2} = \sum_{i=1}^m \frac{q_i n_i \mu_i^2 B_z}{1 + (\mu_i B_z)^2}, \tag{4}$$

With the convention that q_i and μ_i carry the same sign. From the conductivity tensor equation,

$$\mathbf{J} = \begin{pmatrix} \sigma_{xx} & \sigma_{xy} \\ -\sigma_{xy} & \sigma_{xx} \end{pmatrix} \mathbf{E} \iff \begin{pmatrix} R_{xx} & R_{xy} \\ -R_{xy} & R_{xx} \end{pmatrix} \mathbf{J} = \mathbf{E}, \tag{5}$$

where the longitudinal and transverse resistances are expressed as:

$$R_{xx}(B_z) = \frac{\sigma_{xx}(B_z)}{\sigma_{xx}^2(B_z) + \sigma_{xy}^2(B_z)}, \tag{6}$$

$$R_{xy}(B_z) = \frac{\sigma_{xy}(B_z)}{\sigma_{xx}^2(B_z) + \sigma_{xy}^2(B_z)}. \tag{7}$$

In the case of two carrier species, the resistance tensor becomes:

$$R_{xx} = \frac{\sigma_1(1 + (\mu_2 B_z)^2) + \sigma_2(1 + (\mu_1 B_z)^2)}{\sigma_1^2(1 + (\mu_2 B_z)^2) + \sigma_1 \sigma_2(1 + (\mu_1 \mu_2 B_z)^2) + \sigma_2^2(1 + (\mu_1 B_z)^2)}; \tag{8}$$

$$R_{xy} = \frac{\sigma_1 \mu_1 B_z(1 + (\mu_2 B_z)^2) + \sigma_2 \mu_2 B_z(1 + (\mu_1 B_z)^2)}{\sigma_1^2(1 + (\mu_2 B_z)^2) + \sigma_1 \sigma_2(1 + (\mu_1 \mu_2 B_z)^2) + \sigma_2^2(1 + (\mu_1 B_z)^2)}. \tag{9}$$

The polynomial expansion of R_{xx} and R_{xy} in powers of B_z can be expressed as⁴⁹:

$$R_{xx}(B_z) = \frac{c_0 = \frac{1}{\sigma}}{q_1 n_1 \mu_1 + q_2 n_2 \mu_2} + \frac{c_2}{(q_1 n_1 \mu_1 + q_2 n_2 \mu_2)^3} B_z^2 - \frac{c_4 = c_3^2/c_2}{q_1 q_2 n_1 n_2 \mu_1^3 \mu_2^3 (q_1 n_1 + q_2 n_2)^2 (\mu_1 - \mu_2)^2} B_z^4 + \dots, \tag{10}$$

$$R_{xy}(B_z) = \frac{c_1 = R_H}{(q_1 n_1 \mu_1 + q_2 n_2 \mu_2)^2} B_z - \frac{c_3}{(q_1 n_1 \mu_1 + q_2 n_2 \mu_2)^4} (\mu_1 - \mu_2)^2 B_z^3 + \frac{c_5 = c_3^3/c_2^2}{(q_1 n_1 \mu_1 + q_2 n_2 \mu_2)^6} (\mu_1 - \mu_2)^2 B_z^5 + \dots, \tag{11}$$

Here the R_{xx} is even and R_{xy} is odd polynomial magnetic field dependence, respectively. The expansion coefficient c_j in Eqs. 10 and 11 satisfies a recursive condition:

$$c_{j \geq 2} = \frac{c_3^{j-2}}{c_2^{j-3}} = \frac{R_H^j}{R_{sh}^{j-1}} \frac{\beta(1-\beta)(\gamma-1)^2 \gamma^{j-1}}{(1+\beta(\gamma^2+1))^j} \sim 1. \tag{12}$$

Such that R_{xx} and in Eqs. 10 and 11 can be equivalently expressed (without truncating the expansions) as:

$$R_{xx}(B_z) = c_0 + \frac{c_2 B_z^2}{1 + \left(\frac{c_3}{c_2} B_z\right)^2}, \tag{13}$$

$$R_{xy}(B_z) = c_1 B_z - \frac{c_3 B_z^3}{1 + \left(\frac{c_3}{c_2} B_z\right)^2}, \tag{14}$$

The band-resolved densities and mobilities are obtained from the c_{0-3} coefficients by:

$$n_{1,2} = \frac{2c_2^3 - c_1 c_2 c_3 + c_3(c_0 c_3 \pm \text{sgn}(q_{1,2}) c^*)}{2q_{1,2}(c_1 c_3 - c_2^2) c^*}, \tag{15}$$

$$\mu_{1,2} = \frac{c_1 c_2 + c_0 c_3 \mp \text{sgn}(q_{1,2}) c^*}{2c_0 c_2}, \tag{16}$$

where,

$$c^* = \sqrt{c_2^2(c_1^2 + 4c_0 c_2) - 2c_0 c_1 c_2 c_3 + c_0^2 c_3^2}. \tag{17}$$

Module preparation and cooling ΔT measurement

Copper contact layers were deposited onto the samples using ion beam deposition, resulting in a Cu/Bi_{0.88}Sb_{0.12} interface with remarkably low interfacial electrical resistivity (3.7 $\mu\Omega\text{-cm}^2$) and interfacial thermal resistivity (0.14 $\text{mm}^2\text{-K}\cdot\text{W}^{-1}$), respectively (Supplementary Fig. 22). The electrode-plated Bi_{0.88}Sb_{0.12} samples were then diced into square legs measuring $0.9 \times 0.9 \times 3 \text{ mm}^3$. Similarly, the commercial p-type Bi_{0.5}Sb_{1.5}Te₃ materials (Supplementary Fig. 23) were cut into square legs with an optimized area of $1.3 \times 1.3 \text{ mm}^2$ and the same length.

Utilizing these two types of legs, we fabricated a uni-couple single-stage thermoelectric module. The temperature difference was measured using a TTMS (Multifields Tech.). One side of the connected current leads, as the hot end, was attached to the constant-temperature heat sink on the sample platform, as shown in the inset of Fig. 1b. PT-100 temperature sensors were affixed to both the cold and hot ends to measure the temperatures at these locations.

Virtual crystal approximation and lattice parameters

The thermoelectric transport properties of the $\text{Bi}_{0.88}\text{Sb}_{0.12}$ alloy are investigated using first-principles calculations, performed with the Quantum ESPRESSO⁵⁰, EPW⁵¹, and ShengBTE^{52,53} packages. In the following sections, we introduce the fundamental theory and computational details for the electron-phonon, electron-alloy, phonon-phonon, and phonon-alloy interactions.

In the density-functional theory (DFT) calculations, a fully relativistic norm-conserving pseudopotential with the Perdew-Zunger parameterization of the local density approximation exchange-correlation functional⁵⁴ is used for both Bi and Sb. The pseudopotential for the $\text{Bi}_{0.88}\text{Sb}_{0.12}$ is reconstructed by mixing 88% Bi and 12% Sb, based on the virtual crystal approximation (VCA)⁵⁵. Spin-orbit coupling is incorporated into the DFT calculations, and the plane-wave cut-off energy is set to 80 Ry on an $18 \times 18 \times 18$ uniform \mathbf{k} -grid mesh in momentum space. Convergence is achieved in the self-consistent calculations when the estimated energy error is less than 10^{-12} Ry. The optimized lattice constant is 4.6816 Å with an oblique angle of 57.9509° in a rhombohedral crystal structure, and the positions of the two basis atoms are (0, 0, 0) and (0.4702, 0.4702, 0.4702) in crystal coordinates. For comparison, the optimized lattice constants and angles are 4.7042 Å and 57.9874° for Bi, and 4.4813 Å and 57.9180° for Sb. The lattice constant of the $\text{Bi}_{0.88}\text{Sb}_{0.12}$ virtual crystal is close to the average lattice constant of Bi and Sb, which is consistent with Vegard's law, validating the applicability of VCA⁵⁶.

Electron-phonon interaction

The electron-phonon interaction is initially determined by the phonon perturbed potential due to atomic displacements, denoted as $\delta V_{p\mathbf{q}}(\mathbf{r})$, where \mathbf{q} and p represent the wavevector and branch index of a phonon, respectively, and \mathbf{r} denotes the real-space position. The electron-phonon coupling matrix is given by⁵⁷:

$$g_{mnp}(\mathbf{k}, \mathbf{q}) = \left(\frac{\hbar}{2m_0\omega_{p\mathbf{q}}} \right)^{1/2} \langle m\mathbf{k} + \mathbf{q}, l, \delta V_{p\mathbf{q}}(\mathbf{r}), l, n\mathbf{k} \rangle, \quad (18)$$

where m_0 is a reference mass; ω is the phonon frequency; \mathbf{k} is the electron wavevector; n and m represent the index of the initial and final electron bands, respectively. Using this coupling matrix, the electron scattering rate due to phonons can be calculated by:

$$\frac{1}{\tau_{nk}^{\text{e-ph}}} = \frac{2\pi}{\hbar} \sum_{m,p} \int \frac{d\mathbf{q}}{\Omega_{\text{BZ}}} |g_{mnp}(\mathbf{k}, \mathbf{q})|^2 \times \left[\begin{aligned} & (f_{m\mathbf{k}+\mathbf{q}} + n_{p\mathbf{q}}) \delta(\varepsilon_{n\mathbf{k}} - \varepsilon_{m\mathbf{k}+\mathbf{q}} + \hbar\omega_{p\mathbf{q}}) \\ & + (1 - f_{m\mathbf{k}+\mathbf{q}} - n_{p\mathbf{q}}) \delta(\varepsilon_{n\mathbf{k}} - \varepsilon_{m\mathbf{k}+\mathbf{q}} - \hbar\omega_{p\mathbf{q}}) \end{aligned} \right], \quad (19)$$

where Ω_{BZ} is the volume of the first Brillouin zone; ε is the electron energy; f and n represent the Fermi-Dirac and Bose-Einstein distributions, respectively.

The electron Hamiltonian of the $\text{Bi}_{0.88}\text{Sb}_{0.12}$ virtual crystal was computed on a $12 \times 12 \times 12$ \mathbf{k} -grid mesh using non-self-consistent DFT calculations performed on the Quantum ESPRESSO package. The dynamical matrix and phonon perturbed potential were computed on a $6 \times 6 \times 6$ \mathbf{q} -grid mesh using density-functional perturbation theory (DFPT). In the phonon calculations, the threshold for self-consistency was set to 10^{-18} Ry. The DFT and DFPT results were then interpolated onto a $140 \times 140 \times 140$ mesh to compute the electron and phonon eigenvalues and the electron-phonon coupling matrix using the EPW package. Finally, the electron-phonon scattering rates were obtained on this dense mesh, and the results are shown in Fig. 2d and Supplementary Fig. 8.

Electron-alloy interaction

To compute electron-alloy scattering rates, we follow the method proposed by Murphy-Armando and Fahy⁵⁸, which provides a fully first-principles framework based on the VCA for random binary substitutional alloys. In this method, the coupling matrix due to alloy disorder is given by:

$$g_{mna\beta}(\mathbf{k}, \mathbf{k}') = N_{\text{sc}} \langle m\mathbf{k}' | \Delta V_{\alpha}(\mathbf{r}) | n\mathbf{k} \rangle - N_{\text{sc}} \langle m\mathbf{k}' | \Delta V_{\beta}(\mathbf{r}) | n\mathbf{k} \rangle, \quad (20)$$

where N_{sc} is the total number of virtual atoms in the supercell; $\Delta V_{\alpha}(\mathbf{r})$ is the perturbed potential due to a type- α atom. It is determined by the difference between the bare potential of the virtual crystal supercell and the supercell where one virtual atom is replaced by a type- α atom, i.e.,

$$\Delta V_{\alpha}(\mathbf{r}) = V_{\alpha}(\mathbf{r}) - V_{\text{virtual}}(\mathbf{r}). \quad (21)$$

The electron scattering rate due to alloy disorders is calculated by⁵⁸

$$\frac{1}{\tau_{nk}^{\text{e-al}}} = \frac{2\pi x(1-x)}{\hbar N_{\text{sc}}} \sum_m \int \frac{d\mathbf{k}'}{\Omega_{\text{BZ}}} |g_{mn}(\mathbf{k}, \mathbf{k}')|^2 \delta(\varepsilon_{n\mathbf{k}} - \varepsilon_{m\mathbf{k}'}), \quad (22)$$

where x is the alloy composition ratio, which can be 0.88 or 0.12 in this study. The delta function ensures energy conservation in the electron-alloy scattering process, calculated using the tetrahedral smearing technique⁵⁹.

The alloy scattering rates were computed using our in-house modified version of the Quantum ESPRESSO package. A supercell is required to calculate the coupling matrix, as alloy disorder perturbs the potential of surrounding atoms. Although this perturbation is localized, a single primitive cell may not sufficiently exclude interference between two disorder sites. For $\text{Bi}_{0.88}\text{Sb}_{0.12}$, a $2 \times 2 \times 2$ supercell containing 16 virtual atoms with an $8 \times 8 \times 8$ \mathbf{k} -grid mesh in momentum space was employed. The plane-wave cut-off energy and convergence threshold are the same as those used in crystal optimization. A virtual atom was replaced by Bi or Sb to compute $V_{\alpha}(\mathbf{r})$, and then was subtracted from $V_{\text{virtual}}(\mathbf{r})$ to obtain the perturbed potentials on a $109 \times 109 \times 109$ mesh in real space. This supercell was large enough since the perturbed potentials decay to approximately zero within 2.0 Bohr, as shown in Supplementary Fig. 4. The electron-alloy and hole-alloy scattering rates were computed for 1800 \mathbf{k} points, each considering 20 electron bands from the lowest conduction and highest valence bands, resulting in the calculation of scattering rates for 36000 electron states. The obtained alloy scattering rates were interpolated to the $140 \times 140 \times 140$ \mathbf{k} -grid mesh according to the electron energy, to match the resolution of the electron-phonon scattering rates. The DFT and interpolation results for the alloy scattering rates are shown in Fig. 2d and Supplementary Fig. 8.

Phonon-phonon and phonon-alloy interactions

The anharmonicity of the lattice is one of the main causes of thermal resistance in solid materials. Atomic vibrations are inherently anharmonic, and deviations from harmonic forces correspond to the intensity of phonon scattering. As a result, the coupling matrix for phonon-phonon scattering is related to the higher-order terms of the force constants and is given by^{52,53}:

$$\mathcal{M}_{pp'p''}(\mathbf{q}, \mathbf{q}', \mathbf{q}'') = \sum_{i,j,k} \sum_{\alpha,\beta,\gamma} \Phi_{ijk}^{\alpha\beta\gamma} \frac{\xi_{i,p\mathbf{q}}^{\alpha} \xi_{j,p'\mathbf{q}'}^{\beta} \xi_{k,p''\mathbf{q}''}^{\gamma}}{\sqrt{8M_i M_j M_k \omega_{p\mathbf{q}} \omega_{p'\mathbf{q}'} \omega_{p''\mathbf{q}''}}} e^{i\mathbf{q} \cdot \mathbf{r}_j} e^{i\mathbf{q}'' \cdot \mathbf{r}_k}, \quad (23)$$

$$\mathcal{N}_{pp'p''p'''}(\mathbf{q}, \mathbf{q}', \mathbf{q}'', \mathbf{q}''') = \sum_{i,j,k,l} \sum_{\alpha,\beta,\gamma,\theta} \Phi_{ijkl}^{\alpha\beta\gamma\theta} \frac{\xi_{i,pq}^\alpha \xi_{j,p'q'}^\beta \xi_{k,p''q''}^\gamma \xi_{l,p'''q'''}^\theta}{\sqrt{16M_i M_j M_k M_l \omega_{pq} \omega_{p'q'} \omega_{p''q''} \omega_{p'''q'''}}} \times e^{i\mathbf{q}' \cdot \mathbf{r}_j} e^{i\mathbf{q}'' \cdot \mathbf{r}_k} e^{i\mathbf{q}''' \cdot \mathbf{r}_l}, \quad (24)$$

where Φ represents the third- and fourth-order force constants; α, β , and γ are Cartesian coordinates; i, j, k , and l are atomic indices in the system; ξ is the phonon eigenfunction; M is the atomic mass, and \mathbf{r} is the position of a basis atom relative to the lattice point. The three-phonon and four-phonon scattering rates can be obtained by^{52,53}:

$$\frac{1}{\tau_{pq}^{3-ph}} = \frac{2\pi}{\hbar N_{\mathbf{q}}} \sum_{p', p''} \int \frac{d\mathbf{q}'}{\Omega_{\text{BZ}}} \left[\begin{aligned} & |\mathcal{M}|^2 (n_{p'q'} - n_{p''q''}) \\ & \times \delta(\hbar\omega_{pq} - \hbar\omega_{p'q'} + \hbar\omega_{p''q''}) \\ & + \frac{1}{2} |\mathcal{M}|^2 (n_{p'q'} + n_{p''q''} + 1) \\ & \times \delta(\hbar\omega_{pq} - \hbar\omega_{p'q'} - \hbar\omega_{p''q''}) \end{aligned} \right], \quad (25)$$

$$\frac{1}{\tau_{pq}^{4-ph}} = \frac{2\pi}{N_{\mathbf{q}} N_{\mathbf{q}'}} \sum_{p', p'', p'''} \int \frac{d\mathbf{q}'}{\Omega_{\text{BZ}}} \int \frac{d\mathbf{q}''}{\Omega_{\text{BZ}}} \times \left[\begin{aligned} & \frac{1}{2} |\mathcal{N}|^2 (1 + n_{p'q'}) (1 + n_{p''q''}) n_{p'''q'''} \delta(\hbar\omega_{pq} + \hbar\omega_{p'q'} + \hbar\omega_{p''q''} - \hbar\omega_{p'''q'''}) \\ & + \frac{1}{2} |\mathcal{N}|^2 (1 + n_{p'q'}) n_{p''q''} n_{p'''q'''} \delta(\hbar\omega_{pq} + \hbar\omega_{p'q'} - \hbar\omega_{p''q''} - \hbar\omega_{p'''q'''}) \\ & + \frac{1}{6} |\mathcal{N}|^2 n_{p'q'} n_{p''q''} n_{p'''q'''} \delta(\hbar\omega_{pq} - \hbar\omega_{p'q'} - \hbar\omega_{p''q''} - \hbar\omega_{p'''q'''}) \end{aligned} \right] \quad (26)$$

For the phonon-alloy interaction, the scattering matrix is determined by the Pearson coefficients, which depend on the alloy composition ratio and the mass of the virtual atom, and is given by^{52,53}:

$$\mathcal{P}(i) = \sum_s x_s(i) \left[\frac{1 - M_s(i)}{M_{VCA}} \right], \quad (27)$$

where s loops all types of alloy atoms. The phonon-alloy scattering rate is then obtained by:

$$\frac{1}{\tau_{pq}^{ph-al}} = \frac{1}{N} \sum_{p', q'} \frac{\pi \omega_{pq}^2}{2} \left[\sum_i \mathcal{P}(i) |\langle p\mathbf{q}, i, p'\mathbf{q}' \rangle|^2 \delta(\omega_{pq} - \omega_{p'q'}) \right]. \quad (28)$$

The harmonic force constants were computed using DFPT, along with the dynamical matrix and phonon perturbed potential. The higher-order force constants were calculated using supercells within the Quantum ESPRESSO package. A $4 \times 4 \times 4$ supercell with a force cutoff radius extending to the ninth nearest neighbor was used for obtaining the third-order constants. The fourth-order constants, being more localized, were calculated using a $3 \times 3 \times 3$ supercell with a force cutoff radius extending to the fourth nearest neighbor. Phonon-phonon and phonon-alloy scattering rates were computed using the ShengBTE code on a $40 \times 40 \times 40$ \mathbf{q} -grid mesh. The calculated three-phonon, four-phonon, and phonon-alloy scattering rates are shown in Fig. 2c and Supplementary Fig. 6.

Thermoelectric transport properties

The thermoelectric transport properties are calculated according to the Onsager reciprocal relations⁶⁰:

$$L_{11} = -\frac{g_e e^2}{\Omega N_{\mathbf{k}}} \sum_{nk} v_{nk}^\alpha v_{nk}^\beta \tau_{nk}^{\text{total}} \frac{\partial f_{nk}}{\partial \epsilon_{nk}}, \quad (29)$$

$$L_{12} = \frac{g_e e}{\Omega N_{\mathbf{k}} T} \sum_{nk} (\epsilon_{nk} - \epsilon_f) v_{nk}^\alpha v_{nk}^\beta \tau_{nk}^{\text{total}} \frac{\partial f_{nk}}{\partial \epsilon_{nk}}, \quad (30)$$

$$L_{21} = \frac{g_e e}{\Omega N_{\mathbf{k}}} \sum_{nk} (\epsilon_{nk} - \epsilon_f) v_{nk}^\alpha v_{nk}^\beta \tau_{nk}^{\text{total}} \frac{\partial f_{nk}}{\partial \epsilon_{nk}}, \quad (31)$$

$$L_{22} = -\frac{g_e}{\Omega N_{\mathbf{k}} T} \sum_{nk} (\epsilon_{nk} - \epsilon_f)^2 v_{nk}^\alpha v_{nk}^\beta \tau_{nk}^{\text{total}} \frac{\partial f_{nk}}{\partial \epsilon_{nk}}. \quad (32)$$

where $N_{\mathbf{k}}$ is the number of \mathbf{k} grids; Ω is the volume of the primitive cell; ϵ_f is the Fermi energy, determined by the experimental carrier concentration and DFT band structure. The total scattering rate is evaluated using Matthiessen's rule. In this study, we have

$$\frac{1}{\tau_{nk}^{\text{total}}} = \frac{1}{\tau_{nk}^{e-ph}} + \frac{1}{\tau_{nk}^{e-al}}, \quad (33)$$

$$\frac{1}{\tau_{pq}^{\text{total}}} = \frac{1}{\tau_{pq}^{3-ph}} + \frac{1}{\tau_{pq}^{4-ph}} + \frac{1}{\tau_{pq}^{ph-al}}, \quad (34)$$

for electron and phonon, respectively. Using these scattering rates and group velocities, the electrical conductivity, Seebeck coefficient, electrical thermal conductivity, and bipolar thermal conductivity are calculated as follows

$$\sigma = -L_{11}, \quad (35)$$

$$S = \frac{L_{12}}{L_{11}}, \quad (36)$$

$$\kappa_{ele} = L_{11} - \frac{L_{21} L_{12}}{L_{11}}, \quad (37)$$

$$\kappa_{bip} = \left(L_{21}^e \frac{L_{11}^h}{L_{11}^e} - L_{21}^h \right) \frac{L_{12}^e}{L_{11}} + \left(L_{21}^h \frac{L_{11}^e}{L_{11}^h} - L_{21}^e \right) \frac{L_{12}^h}{L_{11}}. \quad (38)$$

The superscripts e and h represent the contributions from the conduction (electron) and valence (hole) bands, respectively, while values without a superscript represent the total contribution.

The lattice thermal conductivity is calculated as⁶⁰

$$\kappa_{lat} = \frac{1}{\Omega N_{\mathbf{q}}} \sum_{pq} \hbar \omega_{pq} v_{pq}^\alpha v_{pq}^\beta \tau_{pq}^{\text{tot}} \frac{\partial n_{pq}}{\partial T}. \quad (39)$$

where $N_{\mathbf{q}}$ is the number of \mathbf{q} grids. The computed thermoelectric transport properties of $\text{Bi}_{0.88}\text{Sb}_{0.12}$ along the binary and trigonal directions at different temperatures are shown in Supplementary Figs. 9 and 10.

The electron and phonon MFPs are, respectively, calculated by

$$\lambda_{nk} = |\mathbf{v}_{nk}| \tau_{nk}^{\text{tot}}, \quad (40)$$

$$\lambda_{pq} = |\mathbf{v}_{pq}| \tau_{pq}^{\text{tot}}. \quad (41)$$

The lower and upper characteristic MFP are defined by the values corresponding to normalized accumulations of 0.1 and 0.9, respectively. This range encompasses the MFPs of electrons and phonons

that contribute approximately 80% of the total electrical and lattice thermal conductivity.

Data availability

All data are available in the manuscript or the supplementary information.

References

- Terada, N. & Mamiya, H. High-efficiency magnetic refrigeration using holmium. *Nat. Commun.* **12**, 1212 (2021).
- Liu, J., Gottschall, T., Skokov, K. P., Moore, J. D. & Gutfleisch, O. Giant magnetocaloric effect driven by structural transitions. *Nat. Mater.* **11**, 620–626 (2012).
- Ma, R. et al. Highly efficient electrocaloric cooling with electrostatic actuation. *Science* **357**, 1130–1134 (2017).
- Meng, Y. et al. A cascade electrocaloric cooling device for large temperature lift. *Nat. Energy* **5**, 996–1002 (2020).
- Qian, S. et al. High-performance multimode elastocaloric cooling system. *Science* **380**, 722–727 (2023).
- Zhang, S. et al. Solid-state cooling by elastocaloric polymer with uniform chain-lengths. *Nat. Commun.* **13**, 9 (2022).
- Anderegg, L. et al. Laser cooling of optically trapped molecules. *Nat. Phys.* **14**, 890–893 (2018).
- Schreck, F. & Druten, K. V. Laser cooling for quantum gases. *Nat. Phys.* **17**, 1296–1304 (2021).
- Pourkiaei, S. M. et al. Thermoelectric cooler and thermoelectric generator devices: a review of present and potential applications, modeling and materials. *Energy* **186**, 115849 (2019).
- He, R., Schierning, G. & Nielsch, K. Thermoelectric devices: a review of devices, architectures, and contact optimization. *Adv. Mater. Technol.* **3**, 1700256 (2018).
- Snyder, G. J. & Toberer, E. S. Complex thermoelectric materials. *Nat. Mater.* **7**, 105–114 (2008).
- Poudel, B. et al. High-thermoelectric performance of nanostructured bismuth antimony telluride bulk alloys. *Science* **320**, 634–638 (2008).
- Pei, J., Cai, B., Zhuang, H.-L. & Li, J.-F. Bi₂Te₃-based applied thermoelectric materials: research advances and new challenges. *Nat. Sci. Rev.* **7**, 1856–1858 (2020).
- Mamur, H., Bhuiyan, M. R. A., Korkmaz, F. & Nil, M. A review on bismuth telluride (Bi₂Te₃) nanostructure for thermoelectric applications. *Renew. Sustain. Energy Rev.* **82**, 4159–4169 (2018).
- Zhao, H. et al. Dramatic thermal conductivity reduction by nanostructures for large increase in thermoelectric figure-of-merit of FeSb₂. *Appl. Phys. Lett.* **99**, 163101 (2011).
- Amato, A. et al. Thermodynamic and transport-properties of CeCu₆. *J. Low. Temp. Phys.* **68**, 371–397 (1987).
- Wang, G., Yang, J. & Zhao, H. Mg₃(Bi, Sb)₂-based thermoelectric modules towards near-room temperature cooling and power generation. *J. Materomics* **8**, 1218–1221 (2022).
- Chen, N. et al. Improved figure of merit (z) at low temperatures for superior thermoelectric cooling in Mg₃(Bi,Sb)₂. *Nat. Commun.* **14**, 4932 (2023).
- Chung, D. Y. et al. CsBi₄Te₆: a high-performance thermoelectric material for low-temperature applications. *Science* **287**, 1024–1027 (2000).
- Lenoir, B., Cassart, M., Michenaud, J. P., Scherrer, H. & Scherrer, S. Transport properties of Bi-rich Bi-Sb alloys. *J. Phys. Chem. Solids* **57**, 89–99 (1996).
- Lenoir, B., Dauscher, A., Cassart, M., Ravich, Y. I. & Scherrer, H. Effect of antimony content on the thermoelectric figure of merit of Bi_{1-x}Sb_x alloys. *J. Phys. Chem. Solids* **59**, 129–134 (1998).
- Chao, P. W., Chu, H. T. & Kao, Y. H. Nonlinear band-parameter variations in dilute bismuth-antimony alloys. *Phys. Rev. B* **9**, 4030–4034 (1974).
- Kraak, W., Oelgart, G., Schneider, G. & Herrmann, R. Semi-conductor-semi-metal transition in bi¹-xsb^x alloys with x greater-than-or-equal-to 0.22. *Phys. Status Solidi B Basic Res.* **88**, 105–110 (1978).
- Vecchi, M. P. & Dresselhaus, M. S. Temperature-dependence of band parameters of bismuth. *Phys. Rev. B* **10**, 771–774 (1974).
- Okamoto, H. Bi-Sb (Bismuth-Antimony). *J. Phase Equilib. Diff.* **33**, 493–494 (2012).
- Kitagawa, H., Noguchi, H., Kiyabu, T., Itoh, M. & Noda, Y. Thermoelectric properties of Bi-Sb semiconducting alloys prepared by quenching and annealing. *J. Phys. Chem. Solids* **65**, 1223–1227 (2004).
- Zhong, L., Wang, J., Sheng, H., Zhang, Z. & Mao, S. X. Formation of monatomic metallic glasses through ultrafast liquid quenching. *Nature* **512**, 177 (2014).
- Zemskov, V. S., Belaya, A. D., Beluy, U. S. & Kozhemyakin, G. N. Growth and investigation of thermoelectric properties of Bi-Sb alloy single crystals. *J. Cryst. Growth* **212**, 161–166 (2000).
- Yim, W. M., Fitzke, E. V. & Rosi, F. D. Thermoelectric properties of Bi₂Te₃-Sb₂Te₃-Sb₂Se₃ pseudo-ternary alloys in the temperature range 77 to 300° K. *J. Mater. Sci.* **1**, 52–65 (1966).
- Sidorenko, N., Parashchuk, T., Maksymuk, M. & Dashevsky, Z. Development of cryogenic cooler based on n-type Bi-Sb thermoelectric and HTSC. *Cryogenics* **112**, 103197 (2020).
- Fee, M. G. Peltier refrigerator using a high-T(°C) superconductor. *Appl. Phys. Lett.* **62**, 1161–1163 (1993).
- Alam, A. Phonon transport in disordered alloys: a multiple-scattering approach. *Phys. Rev. B* **104**, 104202 (2021).
- Tian, Z. et al. Phonon conduction in PbSe, PbTe, and PbTe_{1-x}Se_x from first-principles calculations. *Phys. Rev. B* **85**, 184303 (2012).
- Zhou, W. et al. Effect of four-phonon interaction on phonon thermal conductivity and mean-free-path spectrum of high-temperature phase SnSe. *Appl. Phys. Lett.* **121**, 112202 (2022).
- Liu, T.-H. et al. Electron mean-free-path filtering in Dirac material for improved thermoelectric performance. *Proc. Natl. Acad. Sci. USA.* **115**, 879–884 (2018).
- Esfarjani, K., Chen, G. & Stokes, H. T. Heat transport in silicon from first-principles calculations. *Phys. Rev. B* **84**, 085204 (2011).
- Satterthwaite, C. B. & Ure, R. W. Electrical and thermal properties of Bi₂Te₃. *Phys. Rev.* **108**, 1164–1170 (1957).
- Lee, S. et al. Lattice thermal conductivity of Bi, Sb, and Bi-Sb alloy from first principles. *Phys. Rev. B* **89**, 085206 (2014).
- Lucovsky, G. & White, R. M. Effects of resonance bonding on the properties of crystalline and amorphous semiconductors. *Phys. Rev. B* **8**, 660–667 (1973).
- Zhu, H. et al. Intrinsically low lattice thermal conductivity in natural superlattice (Bi₂)_m(Bi₂Te₃)_n thermoelectric materials. *Chem. Mater.* **33**, 1140–1148 (2021).
- Koopmans, T., Sietsma, J., Zhao, L. & Santofimia, M. J. The thermal stability of quenched and partitioned steel microstructures. *Steel Res. Int.* **92**, 2100290 (2021).
- Luo, T., Wang, S., Li, H. & Tang, X. Low temperature thermoelectric properties of melt spun Bi₈₅Sb₁₅ alloys. *Intermetallics* **32**, 96–102 (2013).
- Wang, J. et al. Cryogenic thermoelectric enhancements in SbCl₃-doped porous Bi_{0.85}Sb_{0.15} alloys. *J. Mater. Chem. C.* **11**, 4056–4069 (2023).
- Malik, K. et al. The effect of quenching from different temperatures on Bi_{0.88}Sb_{0.12} alloy. *J. Phys. Chem. Solids* **91**, 7–12 (2016).
- Hsieh, D. et al. A topological Dirac insulator in a quantum spin Hall phase. *Nature* **452**, 970–975 (2008).
- Gao, S. et al. Enhanced figure of merit in bismuth-antimony fine-grained alloys at cryogenic temperatures. *Sci. Rep.* **9**, 14892 (2019).
- Mangez, J. H., Issi, J. P. & Heremans, J. Transport properties of bismuth in quantizing magnetic-fields. *Phys. Rev. B* **14**, 4381–4385 (1976).

48. Petritz, R. L. Theory of an experiment for measuring the mobility and density of carriers in the space-charge region of a semiconductor surface. *Phys. Rev.* **110**, 1254–1262 (1958).
49. Dill, J. E. et al. Two-carrier model-fitting of Hall effect in semiconductors with dual-band occupation: a case study in GaN two-dimensional hole gas. *J. Appl. Phys.* **137**, 025702 (2025).
50. Giannozzi, P. et al. QUANTUM ESPRESSO: a modular and open-source software project for quantum simulations of materials. *J. Phys. -Condens. Mat.* **21**, 395502 (2009).
51. Ponce, S., Margine, E. R., Verdi, C. & Giustino, F. EPW: electron-phonon coupling, transport and superconducting properties using maximally localized Wannier functions. *Comput. Phys. Commun.* **209**, 116–133 (2016).
52. Li, W., Carrete, J., Katcho, N. A. & Mingo, N. ShengBTE: a solver of the Boltzmann transport equation for phonons. *Comput. Phys. Commun.* **185**, 1747–1758 (2014).
53. Han, Z., Yang, X., Li, W., Feng, T. & Ruan, X. FourPhonon: an extension module to ShengBTE for computing four-phonon scattering rates and thermal conductivity. *Comput. Phys. Commun.* **270**, 108179 (2022).
54. Perdew, J. P. & Zunger, A. Self-interaction correction to density-functional approximations for many-electron systems. *Phys. Rev. B* **23**, 5048–5079 (1981).
55. Nordheim, L. Zur Elektronentheorie der Metalle. II. *Ann. Phys.* **401**, 641–678 (1931).
56. Lee, S., Esfarjani, K., Mendoza, J., Dresselhaus, M. S. & Chen, G. Lattice thermal conductivity of Bi, Sb, and Bi-Sb alloy from first principles. *Phys. Rev. B* **89**, 085206 (2014).
57. Ziman, J. M. *Electrons and Phonons: The Theory of Transport Phenomena in Solids*. <https://doi.org/10.1093/acprof:oso/9780198507796.003.0002> (Oxford University Press, 2001).
58. Murphy-Armando, F. & Fahy, S. First-principles calculation of alloy scattering in GeSi_{1-x}. *Phys. Rev. Lett.* **97**, 096606 (2006).
59. Lambin, P. & Vigneron, J. P. Computation of crystal greens-functions in the complex-energy plane with the use of the analytical tetrahedron method. *Phys. Rev. B* **29**, 3430–3437 (1984).
60. Chen, G. *Nanoscale Energy Transport and Conversion: A Parallel Treatment of Electrons, Molecules, Phonons, and Photons*. <https://doi.org/10.1093/oso/9780195159424.001.0001> (Oxford University Press, 2005).
- measurement, and to Professor Yuan Yao for his assistance with transmission electron microscopy characterization.

Author contributions

H.Z. and X.W. designed this work. T.-H.L. and T.W. carried out simulations and calculations. X.W., X.N., N.C., M.L., Z.L., and Z.F. synthesized the samples. X.W., Q.Z., Q.L., X.Q., and G.L. fabricated the modules and performed the transport property measurements. X.W. performed the XRD, SEM, and EBSD characterizations. J. L performed the TEM characterization. X.W. wrote the original manuscript, which was reviewed and edited by H.Z., T.-H.L., H.Zhu, R.Y., Z.L., and S.W.

Competing interests

H.Z., X.W., and X.N. have filed one Patent Cooperation Treaty patent application (202411236054.8) on the work described here. The remaining authors declare no competing interests.

Additional information

Supplementary information The online version contains supplementary material available at <https://doi.org/10.1038/s41467-025-58491-1>.

Correspondence and requests for materials should be addressed to Te-Huan Liu or Huaizhou Zhao.

Peer review information *Nature Communications* thanks the anonymous, reviewer(s) for their contribution to the peer review of this work. A peer review file is available.

Reprints and permissions information is available at <http://www.nature.com/reprints>

Publisher's note Springer Nature remains neutral with regard to jurisdictional claims in published maps and institutional affiliations.

Open Access This article is licensed under a Creative Commons Attribution-NonCommercial-NoDerivatives 4.0 International License, which permits any non-commercial use, sharing, distribution and reproduction in any medium or format, as long as you give appropriate credit to the original author(s) and the source, provide a link to the Creative Commons licence, and indicate if you modified the licensed material. You do not have permission under this licence to share adapted material derived from this article or parts of it. The images or other third party material in this article are included in the article's Creative Commons licence, unless indicated otherwise in a credit line to the material. If material is not included in the article's Creative Commons licence and your intended use is not permitted by statutory regulation or exceeds the permitted use, you will need to obtain permission directly from the copyright holder. To view a copy of this licence, visit <http://creativecommons.org/licenses/by-nc-nd/4.0/>.

© The Author(s) 2025

Acknowledgements

The authors acknowledge the funding support of the National Key Research and Development Program of China (Grant No. 2022YFB3803900, awarded to H.Z.) and the National Natural Science Foundation of China (Grant No. 52172262 awarded to H.Zhu. and Grant No. 52076089 awarded to T.-H.L.). A portion of this work was carried out at the Synergetic Extreme Condition User Facility (SECUF, <https://cstr.cn/31123.02.SECUF>). The computation is completed in the HPC Platform of Huazhong University of Science and Technology. The authors also express their gratitude to Professor Lidong Zhao and Dr. Tian Gao for their assistance with sound velocity measurements in this work, to Dr. Zhichao Zhao for his assistance with compressive strength